RSC Advances

PAPER

View Article Online
View Journal | View Issue

Cite this: *RSC Adv.*, 2026, **16**, 15398

Luminescent, and thermometric properties of Er^{3+}-activated $NaCaGd(WO_4)_3$ phosphor for solid-state lighting and thermal sensing

Riadh El Bahi,[ab] Kamel Saidi,[cd] Dhouha Baghdedi,[e] Najmeddine Abdelmoula[e] and Mohamed Dammak *[c]

We report the synthesis and comprehensive characterization of Er^{3+}-doped $NaCaGd(WO_4)_3$ phosphors with dopant concentration (0–7%) *via* solid-state reaction methodology. Rietveld refinement of synchrotron X-ray diffraction data confirms a phase-pure tetragonal scheelite structure ($I4_1/a$) with successful lattice-tuned substitution of Gd^{3+} by Er^{3+} ions, with unit cell contraction indicating homogeneous incorporation. Morphological studies *via* scanning electron microscopy demonstrate uniform particle distribution with compact grain morphology. Luminescence analysis reveals vivid green emission (CIE: $x = 0.337$, $y = 0.587$) from $^2H_{11/2}$ and $^4S_{3/2}$ excited states, under 325 nm excitation. The material exhibits exceptional thermometric performance through non-contact fluorescence intensity ratio thermometry over 298–573 K, with Boltzmann-distributed thermal quenching behavior: relative sensitivity peaks at 1.55% K^{-1} near ambient conditions, coupled with an absolute sensitivity of 1.81×10^{-2} K^{-1} and sub-kelvin thermal resolution (±0.15 K at 300 K), values competitive with state-of-the-art rare-earth thermophosphors. The combination of optical stability, tunable green emission from efficient host-sensitization, and sub-kelvin temperature discrimination positions $NaCaGd(WO_4)_3$:Er^{3+} as a bifunctional material for next-generation solid-state lighting, full-color display systems, and non-contact high-precision thermal sensing.

Received 26th January 2026
Accepted 15th March 2026

DOI: 10.1039/d6ra00698a

rsc.li/rsc-advances

1 Introduction

The shielded 4f electronic transitions of trivalent lanthanide ions, which produce sharp emission lines, long luminescence lifetimes, and excellent chemical and thermal stability, have made rare-earth-doped phosphors indispensable in modern optoelectronic technologies, enabling breakthroughs in solid-state lighting, optical communications, biomedical imaging, and non-contact thermometry.[1–4] Among these activators, Er^{3+} ($4f^{11}$) supports versatile luminescence across the ultraviolet, visible, and near-infrared spectral regions.[5] Efficient green-emitting components are crucial for bridging the so-called "green gap" in phosphor-converted white light-emitting diodes (pc-LEDs) and improving both luminous efficacy and color rendering index (CRI). In Er^{3+}-doped systems, intense green emission results from the radiative decay of the thermally coupled $^2H_{11/2}$ and $^4S_{3/2}$ levels to the $^4I_{15/2}$ ground state.[6,7] This small energy separation between these excited states ($\Delta E \approx$ 700–900 cm^{-1}) not only improves color stability in lighting but also serves as the physical foundation for fluorescence intensity ratio (FIR)-based optical thermometry.[8–10] By taking advantage of Boltzmann equilibrium between thermally coupled levels, the FIR technique provides high-precision, non-contact temperature sensing with advantages over conventional thermocouples in harsh or inaccessible environments, including immunity to electromagnetic interference, signal drift, and mechanical constraints.[11] Although improved systems have attained relative sensitivities greater than 1.0% K^{-1},[18–20] the host lattice continues to be the primary determinant of both thermometric performance and luminescence efficiency. While co-doping techniques (*e.g.*, Er^{3+}/Yb^{3+}) are frequently employed to improve near-infrared response and binary hosts like $CaWO_4$ and Y_2O_3 are well-established, recent research has increasingly concentrated on complex multi-cation matrices that allow fine-tuning of crystal field symmetry, phonon energy, and energy transfer pathways. In particular, tri- and quaternary systems have shown better thermal stability and dual-mode sensing capabilities.[12–14]

[a]*Laboratoire de Physique des Matériaux, Faculté des Sciences de Sfax, Département de Physique, Université de Sfax, Sfax, Tunisia*

[b]*Université de Gabès, Département de Physique, Institut Préparatoire aux Études d'Ingénieurs de Gabès, Avenue Omar Ibn El Khattab, 6029 Gabès, Tunisia*

[c]*Laboratoire de Physique Appliquée, Faculté des Sciences de Sfax, Département de Physique, Université de Sfax, BP 1171, Sfax, Tunisia. E-mail: madidammak@yahoo.fr; Mohamed.dammak@fss.usf.tn*

[d]*Université de Sfax, Département de Physique, Institut Préparatoire aux Études d'Ingénieurs de Sfax, 3000 Sfax, Tunisia*

[e]*Laboratory of Multifunctional Materials and Applications (LaMMA), Faculty of Sciences of Sfax, University of Sfax, BP 1171, Sfax 3000, Tunisia*

Tungstate-based materials with scheelite-type structures are particularly attractive due to their strong WO_4^{2-} ligand absorption, efficient host-to-dopant energy transfer, and relatively low phonon energies (~800–900 cm^{-1}), which suppress non-radiative losses.[15–17] While binary tungstates have been extensively studied, quaternary tungstates offer greater structural flexibility for crystal field engineering. In this context, $NaCaGd(WO_4)_3$ presents a compelling tetragonal scheelite framework (space group $I4_1/a$) in which the Gd^{3+} site provides an ideal substitutional environment for Er^{3+} due to matching ionic radii and coordination geometry.

We focus on the intrinsic luminescence and thermometric behavior of Er^{3+} in $NaCaGd(WO_4)_3$, without co-dopants or sensitizers, expanding on recent work in complex molybdate and vanadate systems, where high thermometric sensitivity and structural resilience have been reported.[18,19]

Recent progress in scheelite-type tungstates has further demonstrated their relevance for robust luminescence thermometry, with multiple reports showing that scheelite (or scheelite-like) tungstate lattices provide favorable stability and a tunable crystal-field environment for lanthanide activators. In particular, Er^{3+}/Yb^{3+} co-doped scheelite matrices have been widely explored to enhance upconversion efficiency through sensitizer-mediated energy transfer. However, while Yb^{3+} co-doping improves absorption and emission intensity, it may also introduce additional cross-relaxation channels and concentration-dependent quenching effects that can complicate the intrinsic FIR response. In contrast, single-doped Er^{3+} systems allow a more direct evaluation of host–activator interactions and Boltzmann redistribution between the thermally coupled $^2H_{11/2}$ and $^4S_{3/2}$ levels without sensitizer-induced perturbations.[20–23]

Despite the potential of such quaternary tungstates, systematic investigations of single-doped Er^{3+} systems under near-UV stimulation compatible with commercial LEDs remain scarce. It is vital to understand host–dopant interactions in disordered lattices, and we provide the first complete characterization of Er^{3+}:$NaCaGd(WO_4)_3$ phosphors. We provide a complete investigation of structural characteristics, photoluminescence, and temperature-dependent FIR behavior across a wide range (298–573 K). Our findings reveal that this quaternary host permits efficient green emission, good thermal coupling, and high relative sensitivity (1.55% K^{-1} at 300 K) with sub-kelvin temperature precision (±0.15 K at 300 K).

2 Materials and methods

2.1 Sample synthesis

Polycrystalline $NaCaGd(WO_4)_3$ samples, doped with different amounts of Er^{3+}, were made using a standard solid-state reaction. The starting materials, which were all of high purity, included sodium carbonate (Na_2CO_3, Merck, ≥99.5%), calcium carbonate ($CaCO_3$, Sigma-Aldrich, ≥99.0%), gadolinium oxide (Gd_2O_3, Alfa Aesar, 99.99% purity), tungsten trioxide (WO_3, Sigma-Aldrich, ≥99.8%), and erbium oxide (Er_2O_3, Alfa Aesar, 99.99% purity). These were measured according to stoichiometric ratios, with Er^{3+} doping levels of $x = 1$, 3, 5, and 7 mol% (the mole fraction of Er_2O_3 compared to Gd_2O_3). Before the reaction, all precursor powders were dried at 110 °C for 4 hours to remove any remaining moisture. The dried oxides and carbonates were then mixed in an agate mortar and pestle for 120 minutes to achieve homogeneous distribution. The intimate mixture was placed in a high-alumina crucible and subjected to a multi-step heating profile: (1) calcination at 600 °C for 4 hours (heating rate: 2 °C min^{-1}) to decompose carbonates; (2) intermediate firing at 900 °C for 6 hours (heating rate: 3 °C min^{-1}); and (3) final sintering at 1050 °C for 10 hours (heating rate: 2 °C min^{-1}) in ambient air. After each heating stage, the samples were cooled to room temperature at a controlled rate (1 °C min^{-1}) and subjected to 30 minutes of grinding to promote solid-state diffusion and homogenization. The final white/cream-colored powder products were collected and stored in sealed containers under ambient conditions prior to characterization.

X-ray diffraction (XRD) analyses were carried out under grazing-incidence conditions using a Siemens D8 θ–2θ diffractometer equipped with a Cu Kα radiation source ($\lambda = 0.15418$ nm). The surface morphology of the samples was examined by field-emission scanning electron microscopy (FE-SEM) using a Thermo Scientific Apreo 2 S LoVac instrument. Fourier-transform infrared (FTIR) spectra were obtained at ambient temperature, spanning the 400–4000 cm^{-1} spectral domain, utilizing a PerkinElmer FTIR 1000 spectrometer. Ultraviolet-visible-near-infrared (UV-vis-NIR) absorption measurements were executed with a PerkinElmer Lambda 365 spectrophotometer. Photoluminescence (PL) excitation and emission spectra were collected *via* a Horiba Fluoromax-4P spectrofluorometer, which utilized a xenon arc lamp for excitation. Furthermore, temperature-dependent steady-state emission measurements were performed using a Jobin Yvon HR 320 spectrometer, which was integrated with a temperature-controlled stage and excited by a 325 nm laser source.

3 Results and discussion

3.1 Structural and morphological characterization (XRD and SEM)

X-ray diffraction (XRD) investigation (Fig. 1) verifies that both undoped and Er^{3+}-doped $NaCaGd(WO_4)_3$ samples crystallize in a single-phase tetragonal scheelite structure (space group $I4_1/a$), exhibiting no discernible impurity peaks. All reflections correspond accurately with reference patterns, demonstrating increased phase purity and crystallinity. A systematic displacement of the (112) peak towards elevated 2θ angles with increasing Er^{3+} concentration indicates gradual lattice contraction, along with the replacement of larger Gd^{3+} (0.94 Å) by smaller Er^{3+} ions (0.89 Å, CN = 6). Rietveld refinement of the undoped 3% Er^{3+}-doped sample displays a good degree of consistency between the observed and estimated diffraction patterns, as demonstrated by $R_{wp} = 8.4\%$, $\chi^2 = 1.38$ and $R_{wp} = 7.2\%$, $\chi^2 = 1.18$ respectively. The corrected lattice characteristics, demonstrate a uniform decrease with escalating doping concentration: from $a = 5.289$ Å, $c = 11.643$ Å, $V = 325.48$ Å^3 (undoped) to $a = 5.283$ Å, $c = 11.631$ Å, $V = 325.11$ Å^3 (5 mol%

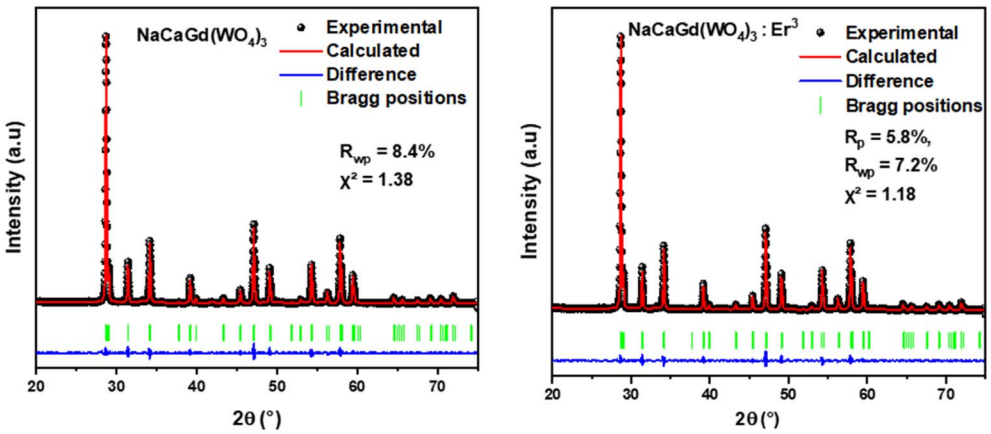

Fig. 1 Rietveld refinement of the powder X-ray diffraction (XRD) patterns of undoped and 3% Er^{3+}-doped $NaCaGd(WO_4)_3$ samples recorded at room temperature. The experimental data (symbols), calculated pattern (solid line), Bragg reflection positions (vertical ticks), and difference profile (bottom line) are shown, confirming the formation of a single-phase scheelite structure and successful incorporation of Er^{3+} ions without secondary phases.

Er^{3+}). This result corroborates the conclusion that Er^{3+} ions are consistently incorporated at the Gd^{3+} lattice sites, with no evidence of secondary phases or ion clustering.

Fig. 2 shows representative SEM micrographs of the $NaCaGd(WO_4)_3$:3% Er^{3+} phosphor. The powder has irregular, angular particles that are typical of solid-state synthesized materials, with particle sizes ranging from 1 to 5 μm. The particle-size distribution is relatively broad (polydisperse), reflecting the grinding and sieving steps inherent in solid-state synthesis; notably, no significant particle agglomeration, indicating effective powder dispersion and handling; the surface morphology appears rough, suggesting incomplete sintering, a useful characteristic for maintaining a high surface area and making luminescence measurements in powder form.

3.2 Fourier-transform infrared spectroscopy (FTIR)

The Fourier-transform infrared (FTIR) spectra of the $NaCaGd(WO_4)_3$:x% Er^{3+} phosphors (x = 1, 3, 5, and 7 mol%) recorded in the range 400–4000 cm^{-1} are presented in Fig. 3. All spectra exhibit the characteristic vibrational features of scheelite-type tungstate lattices, confirming the preservation of the fundamental WO_4^{2-} tetrahedral framework upon Er^{3+} incorporation.[24] This observation is consistent with general studies on tungstate-based materials.[25] The most intense and well-defined absorption band, centered at approximately 840 cm^{-1}, is assigned to the asymmetric stretching vibration ν_3(W–O) of isolated WO_4^{2-} tetrahedra. The sharpness and high intensity of this band indicate a high degree of structural order and minimal distortion of the tetrahedral units.[26] An additional absorption feature observed near 450 cm^{-1} is attributed to symmetric stretching ν_1(W–O) and/or bending ν_4(O–W–O) modes associated with internal vibrations of the WO_4^{2-} groups, which are commonly reported for scheelite-type tungstates.[27–29] A notable feature of the FTIR spectra is their strong invariance with respect to Er^{3+} concentration. The positions, shapes, and relative intensities of all major absorption bands remain essentially unchanged across the investigated doping range. This spectral stability indicates that substitution of Er^{3+} ions for

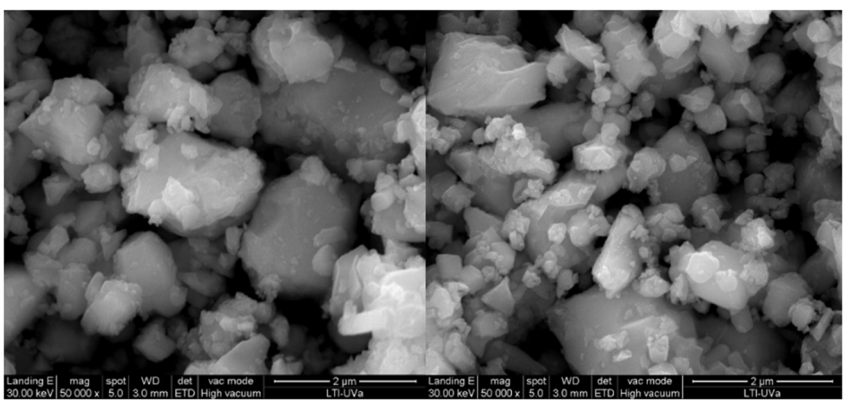

Fig. 2 Scanning electron microscopy (SEM) image of the representative $NaCaGd(WO_4)_3$:3% Er^{3+} phosphor recorded at room temperature, showing irregularly shaped micrometric particles with sizes ranging from approximately 1 to 5 μm, indicating particle agglomeration and heterogeneous grain morphology resulting from the solid-state synthesis process.

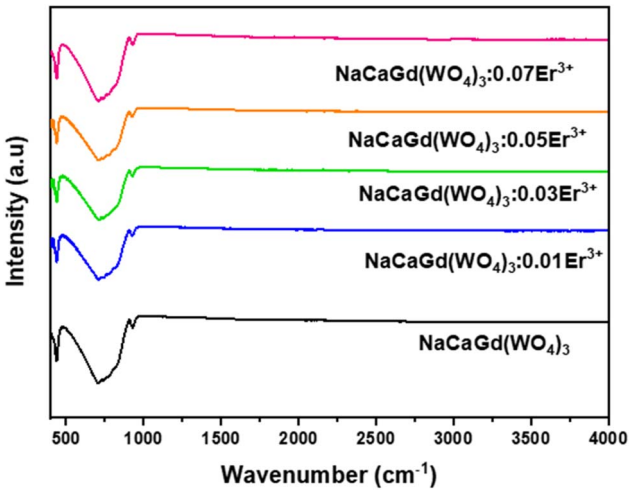

Fig. 3 Fourier-transform infrared (FTIR) spectra of $NaCaGd(WO_4)_3$:*x*% Er^{3+} phosphors (x = 0, 1, 3, 5, and 7 mol%) recorded at room temperature, illustrating the characteristic vibrational modes of the WO_4^{2-} tetrahedral units. The spectra confirm the preservation of the host lattice structure upon Er^{3+} incorporation, with no additional bands associated with secondary phases observed within the detection limits.

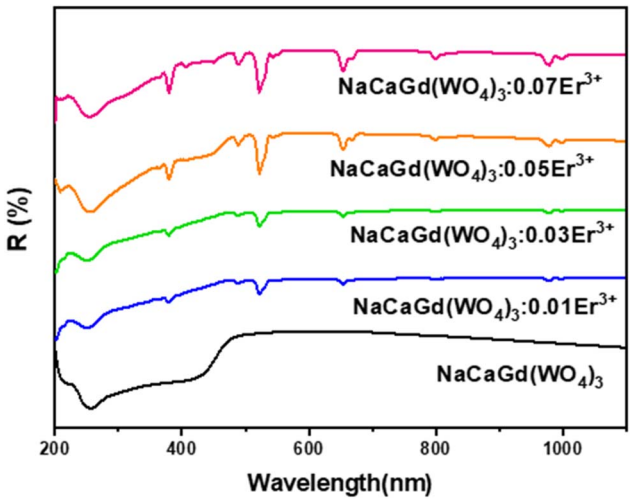

Fig. 4 Diffuse reflectance spectra of $NaCaGd(WO_4)_3$:*x*% Er^{3+} phosphors (x = 0, 1, 3, 5, and 7 mol%) measured at room temperature in the UV-vis region. The spectra reveal the broad host absorption band attributed to $O^{2-} \rightarrow W^{6+}$ charge-transfer transitions in the WO_4^{2-} groups, along with characteristic intra-4f absorption lines of Er^{3+} ions, whose intensity increases with dopant concentration, confirming the successful incorporation of Er^{3+} into the scheelite lattice. Upon doping with Er^{3+}, the reflectance spectrum exhibits characteristic dips at wavelengths associated with intra-4f transitions originating from the $^4I_{15/2}$ ground state: approximately 380 nm, 520 nm ($^4I_{15/2} \rightarrow {}^2H_{11/2}$), 550 nm ($^4I_{15/2} \rightarrow {}^4S_{3/2}$), 650 nm ($^4I_{15/2} \rightarrow {}^4F_{9/2}$), and 980 nm ($^4I_{15/2} \rightarrow {}^4I_{11/2}$).[31,32] The intensities of these spectral features demonstrate a nearly linear correlation with Er^{3+} concentration, suggesting a uniform dopant distribution and the absence of substantial clustering. Notably, a strong absorption feature centered at ~325 nm is observed in both undoped and doped samples, which is assigned to the spin-allowed $^1A_1 \rightarrow {}^1T_1$ ligand-centered transition of the WO_4^{2-} group.[33,34] The intensity of the Er^{3+}-related dips increases linearly with dopant concentration, confirming uniform incorporation without clustering. In this work, 325 nm excitation was selected to leverage efficient host-to-dopant energy transfer from the WO_4^{2-} sensitizer to Er^{3+} ions, enabling intense green upconversion luminescence under near-UV pumping.

Gd^{3+} occurs in a homogeneous and isotropic manner within the cationic sublattice, without inducing detectable perturbations of the WO_4^{2-} tetrahedral network. Such behavior, consistent with the close ionic radii of Er^{3+} and Gd^{3+}, corroborates the conclusions drawn from X-ray diffraction and Rietveld refinement analyses.

A weak and broad absorption band centered around 3500 cm^{-1} is observed in all samples and is attributed to O–H stretching vibrations arising from physically adsorbed water molecules on the powder surface. This feature is frequently encountered in oxide phosphor powders exposed to ambient atmosphere and does not indicate structural hydroxylation or bulk hydration.[30]

Finally, the absence of additional absorption bands in the region's characteristic of CO_3^{2-} or NO_3^- species (1200–1400 cm^{-1}), C=O stretching modes (1600–1800 cm^{-1}), or secondary metal–oxygen vibrations (below 400 cm^{-1}) confirms the high chemical purity of the synthesized phosphors.[25]

3.3 Diffuse reflectance spectroscopy (UV-visible)

Diffuse reflectance spectra for both undoped and Er^{3+}-doped $NaCaGd(WO_4)_3$ samples are presented in Fig. 4, spanning the 250–1100 nm wavelength range. The undoped host material demonstrates substantial reflectance throughout the visible and near-infrared spectra, with a pronounced decrease below approximately 380 nm, which is indicative of the fundamental absorption edge typical of a wide-bandgap tungstate.[26] This wide bandgap corroborates the matrix's high optical transparency within the visible spectrum, thereby minimizing reabsorption losses and facilitating efficient luminescence.

3.4 Photoluminescence and excitation spectroscopy (PL/PLE)

The photoluminescence excitation (PLE) spectrum of $NaCaGd(WO_4)_3$:3% Er^{3+}, monitored at the green emission maximum (λ_{em} = 551 nm, corresponding to the $^4S_{3/2} \rightarrow {}^4I_{15/2}$ transition), is shown in Fig. 5a. A strong, narrow excitation band is observed at about 325 nm, which is clearly assigned to the spin-allowed $^1A_1 \rightarrow {}^1T_1$ ligand-centered transition of the WO_4^{2-} group. This confirms that energy transfer from the tungstate matrix to the Er^{3+} ions is efficient, allowing the $^4S_{3/2}$ level to be populated. Weaker secondary bands are observed at approximately 380 nm, 400 nm, and 450 nm, which probably result from higher-energy charge-transfer states or weak direct 4f–4f transitions.

The photoluminescence excitation (PLE) spectrum of $NaCaGd(WO_4)_3$:3% Er^{3+}, monitored at 551 nm ($^4S_{3/2} \rightarrow {}^4I_{15/2}$ transition), exhibits a dominant narrow excitation band centered at ~325 nm, which is attributed to the spin-allowed $^1A_1$

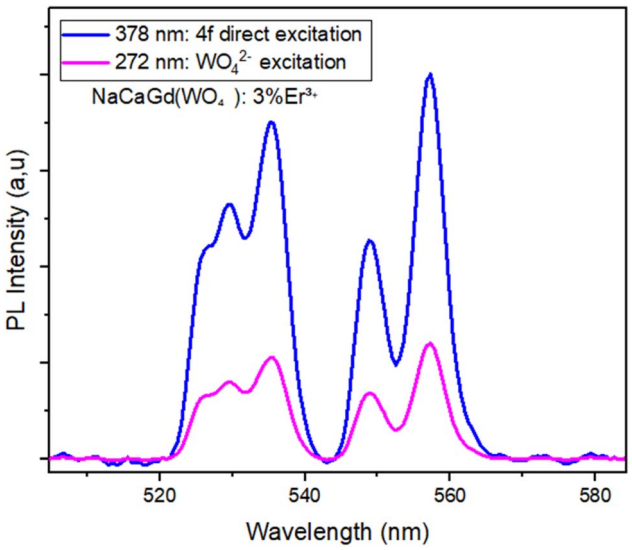

Fig. 5 Photoluminescence emission spectra of $NaCaGd(WO_4)_3$:3-mol% Er^{3+} phosphor recorded under 272 nm (host WO_4^{2-} excitation) and 378 nm (direct Er^{3+} 4f excitation), illustrating the host-to-Er^{3+} energy transfer responsible for the characteristic green emissions ($^2H_{11/2} \rightarrow {}^4I_{15/2}$ and $^4S_{3/2} \rightarrow {}^4I_{15/2}$).

$\rightarrow {}^1T_1$ ligand-to-metal charge-transfer (LMCT) transition within the WO_4^{2-} tetrahedral group. This band corresponds to an $O^{2-} \rightarrow W^{6+}$ charge-transfer excitation and represents a strong absorption channel of the host lattice. Upon UV excitation, the excited WO_4^{2-} group undergoes rapid non-radiative relaxation to lower-lying vibrational levels of the charge-transfer state, followed by energy migration through the lattice and subsequent non-radiative energy transfer to nearby Er^{3+} ions (Fig. 5b).

The efficiency of this host-sensitized mechanism is evidenced by the fact that the excitation intensity at 325 nm is more than an order of magnitude higher than that of the direct 4f–4f excitation of Er^{3+} (*e.g.*, $^4I_{15/2} \rightarrow {}^4S_{3/2}$). This clearly indicates that indirect excitation *via* the WO_4^{2-} charge-transfer band dominates over direct intra-4f absorption, which is parity forbidden and intrinsically weak.

The energy transfer from WO_4^{2-} to Er^{3+} is likely governed by multipolar (dipole–dipole) interactions, facilitated by spectral overlap between the relaxed charge-transfer emission of the tungstate group and higher-lying 4f excited states of Er^{3+}. After energy acceptance, Er^{3+} ions relax non-radiatively to the thermally coupled $^2H_{11/2}$ and $^4S_{3/2}$ levels, from which intense green emission occurs. The schematic energy-level diagram (Fig. 5b) illustrates this sequential process. This mechanism confirms that $NaCaGd(WO_4)_3$ acts not merely as a passive matrix but as an active sensitizing host, significantly enhancing Er^{3+} excitation efficiency under near-UV pumping.

To further evaluate the $WO_4^{2-} \rightarrow Er^{3+}$ host-sensitized energy transfer mechanism, the photoluminescence spectra of the optimized $NaCaGd(WO_4)_3$:3 mol% Er^{3+} phosphor were recorded under two different excitation wavelengths: 272 nm, corresponding to the charge-transfer absorption band of the WO_4^{2-} groups, and 378 nm, associated with the direct 4f excitation of Er^{3+} ions. The resulting emission spectra are presented in Fig. 5.

Under both excitation conditions, the characteristic green emission bands of Er^{3+} ions corresponding to the $^2H_{11/2} \rightarrow {}^4I_{15/2}$ and $^4S_{3/2} \rightarrow {}^4I_{15/2}$ transitions are observed, confirming the efficient population of the emitting levels. The presence of intense Er^{3+} emission under host excitation clearly indicates an energy transfer process from the WO_4^{2-} groups to the Er^{3+} activator ions. The energy transfer efficiency was estimated by comparing the integrated emission intensity of the dominant green band ($^4S_{3/2} \rightarrow {}^4I_{15/2}$) under host and direct excitation using the relation:

$$\eta_{ET} = I_{host}/(I_{host} + I_{direct}) \quad (1)$$

where I_{host} and I_{direct} correspond to the integrated emission intensities obtained under 272 nm and 378 nm excitation, respectively. The calculated efficiency is approximately ~20%, indicating a moderate but effective host-to-Er^{3+} energy transfer process in the $NaCaGd(WO_4)_3:Er^{3+}$ phosphor. This result provides further support for the host-sensitized excitation mechanism inferred from the excitation spectra.

The photoluminescence (PL) emission spectra of $NaCaGd(WO_4)_3:Er^{3+}$ samples with varying dopant concentrations (x = 1, 3, 5, and 7 mol%) under 325 nm excitation are presented in Fig. 5c. All samples exhibit characteristic green emission bands centered at ~528 nm ($^2H_{11/2} \rightarrow {}^4I_{15/2}$) and ~551 nm ($^4S_{3/2} \rightarrow {}^4I_{15/2}$), along with a much weaker red emission band near 660 nm ($^4F_{9/2} \rightarrow {}^4I_{15/2}$).[35,36] The high green-to-red intensity ratio (>10 : 1) confirms the strong potential of this material as an efficient green-emitting phosphor when excited *via* the WO_4^{2-} host absorption.[37,38] The PL intensity shows a clear dependence on Er^{3+} concentration, with non-monotonic behavior directly linked to energy transfer efficiency and concentration quenching. Among the samples, the 3 mol% Er^{3+} sample exhibits the highest emission intensity, identifying it as the optimal doping level. In contrast, the 1 mol% Er^{3+} sample shows significantly weaker emission due to insufficient activator density to effectively harvest the energy transferred from the WO_4^{2-} groups. At higher concentrations, the 5 mol% and 7 mol% samples display reduced PL intensity relative to the 3 mol% sample, indicating the onset of concentration quenching. This is attributed to enhanced Er^{3+}–Er^{3+} interactions, primarily through dipole–dipole cross-relaxation processes.[39,40]

To assess the thermal stability of the phosphor under practical LED operating conditions, we monitored the temperature-dependent PL emission spectra between 300 and 350 K. The integrated green-emission intensity (510–575 nm) decreases only moderately with temperature and remains ~77% at 348 K (≈350 K) compared with 300 K, representing a retention of ~77% of the initial intensity. At 323 K, the intensity retains ~84.2% of its value at 300 K. These results indicate good thermal stability of the emission in the LED-relevant range, which is beneficial for maintaining brightness and ensuring reliable optical readout during device operation.

Repeated PL measurements on powders stored under ambient laboratory conditions for several days showed reproducible spectra, consistent with the generally high chemical stability reported for scheelite-type tungstate hosts.

Absolute photoluminescence quantum yield (PLQY) measurements were performed using an integrating sphere under 325 nm excitation. The optimized $NaCaGd(WO_4)_3$:3-mol% Er^{3+} phosphor exhibits a PLQY value of 25%. This value is consistent with the moderate radiative efficiencies typically reported for Er^{3+}-doped oxide phosphors, where competing non-radiative multiphonon relaxation processes limit the overall emission efficiency under UV excitation.

Additional non-radiative losses may arise from energy migration to defects or reabsorption between neighboring Er^{3+} ions. The observed optimum at 3 mol% Er^{3+} is consistent with typical behavior in rare-earth-doped oxide phosphors, where moderate doping maximizes luminescence by balancing sensitizer-to-activator energy transfer against concentration-induced quenching. Accordingly, the 3 mol% Er^{3+}-doped $NaCaGd(WO_4)_3$ was selected as the reference composition for all subsequent optical and thermometric investigations due to its superior emission performance under 325 nm excitation.

The CIE 1931 chromaticity coordinates of the $NaCaGd(WO_4)_3$:Er^{3+} phosphors were derived from their normalized photoluminescence emission spectra under 325 nm excitation, using conventional photometric techniques. For the optimally doped 3 mol% Er^{3+}, the resulting coordinates are $x = 0.337$, $y = 0.587$, as shown in Fig. 6d. These coordinates position the emission firmly inside the pure green region of the CIE 1931 diagram, close to the spectral locus at ~550–560 nm, consistent with the major contributions from the $^2H_{11/2} \rightarrow {}^4I_{15/2}$ and $^4S_{3/2} \rightarrow {}^4I_{15/2}$ transitions of Er^{3+}. The color purity of this emission is calculated at 88%, indicating that the narrowband character of the f–f transitions yields a color purity substantially greater than that of standard broadband phosphors such as Ce^{3+}:YAG (<50%). The associated correlated color temperature (CCT) of approximately 7500 K is consistent with a cool daylight-white chromaticity, suitable for high-color-fidelity white-light applications. These chromatic features highlight the material's significant potential for solid-state lighting (SSL) applications.[41–43]

To better contextualize the chromatic performance, the obtained coordinates ($x = 0.337$, $y = 0.587$) were compared with standard green emitters commonly used in solid-state lighting. For instance, the commercial terbium-based phosphor (Tb^{3+}-activated materials), widely employed in display and lamp technologies, typically exhibits chromaticity coordinates around ($x \approx 0.36$, $y \approx 0.60$). Similarly, β-SiAlON:Eu^{2+} green phosphors show coordinates near (0.32–0.35, 0.60–0.62), depending on composition. The $NaCaGd(WO_4)_3$:3 mol% Er^{3+} phosphor demonstrates comparable chromaticity positioning within the pure green region while offering a significantly higher color purity (88%) due to the intrinsically narrow 4f–4f transitions of Er^{3+}. Therefore, the present material provides competitive chromatic characteristics relative to standard commercial green phosphors, with the added advantage of temperature-sensitive emission suitable for optical thermometry applications.

4 Optical thermometry

The optical thermometry performance of $NaCaGd(WO_4)_3$:Er^{3+} (3 mol%) was systematically evaluated under 325 nm continuous-wave excitation across a temperature range of 300–600 K (Fig. 6a). As shown in Fig. 6b, the integrated green emission intensity decreases monotonically with increasing temperature a hallmark of thermal quenching. This is due to the enhanced competition between radiative decay and non-radiative relaxation pathways at elevated temperatures. The thermometric mechanism relies on the thermally coupled energy levels (TCLs) of Er^{3+}, specifically the closely spaced $^2H_{11/2}$ and $^4S_{3/2}$ manifolds, which both decay radiatively to the $^4I_{15/2}$ ground state, emitting green light at ~528 nm and ~551 nm, respectively. Due to their small energy separation, these levels are thermally populated according to the Boltzmann distribution.[44,45]

$$\mathrm{LIR} = I_H/I_S = A \cdot \exp(-\Delta E/k_B T) \quad (2)$$

where I_H and I_S are the integrated intensities of the $^2H_{11/2} \rightarrow {}^4I_{15/2}$ and $^4S_{3/2} \rightarrow {}^4I_{15/2}$ transitions, B is calibration constants accounting for transition probabilities and instrumental response, $k_B = 0.695\ \mathrm{cm^{-1}\ K^{-1}}$ is Boltzmann's constant, ΔE is the energy gap between the two TCLs (in $\mathrm{cm^{-1}}$) and T is the absolute temperature (K).

As illustrated in Fig. 5b, the experimental LIR data exhibit excellent agreement with the Boltzmann model fit, yielding $\Delta E = 710\ \mathrm{cm^{-1}}$. This value aligns well with literature reports for Er^{3+}-doped oxides and phosphors employing the same TCL, validating our spectral assignments and confirming the robustness of the thermometric approach. The high quality of the fit ($R^2 > 0.99$) underscores the reliability of this phosphor for precision temperature sensing applications.

Quantifying the responsiveness of the luminescence-based thermometer to temperature fluctuations requires evaluation of two complementary sensitivity parameters. Absolute sensitivity (S_a), defined as the slope of the LIR-temperature relationship, captures the absolute rate of change in the measured parameter per unit temperature increase. Relative sensitivity (S_r), normalized to the LIR value itself, accounts for proportional variations and is particularly useful for comparative assessment across different thermometric strategies.

These metrics are rigorously expressed as:[46–48]

$$S_a = \frac{d\mathrm{LIR}}{dT} \quad (3)$$

$$S_r = \frac{1}{\mathrm{LIR}} \times \frac{\delta \mathrm{LIR}}{\delta T} \times 100\% \quad (4)$$

The material has a maximum relative sensitivity of 1.55% K^{-1} at 300 K, among the greatest reported for Er^{3+}-based optical thermometers, making it especially appropriate for biomedical and physiological applications. At high temperatures, the

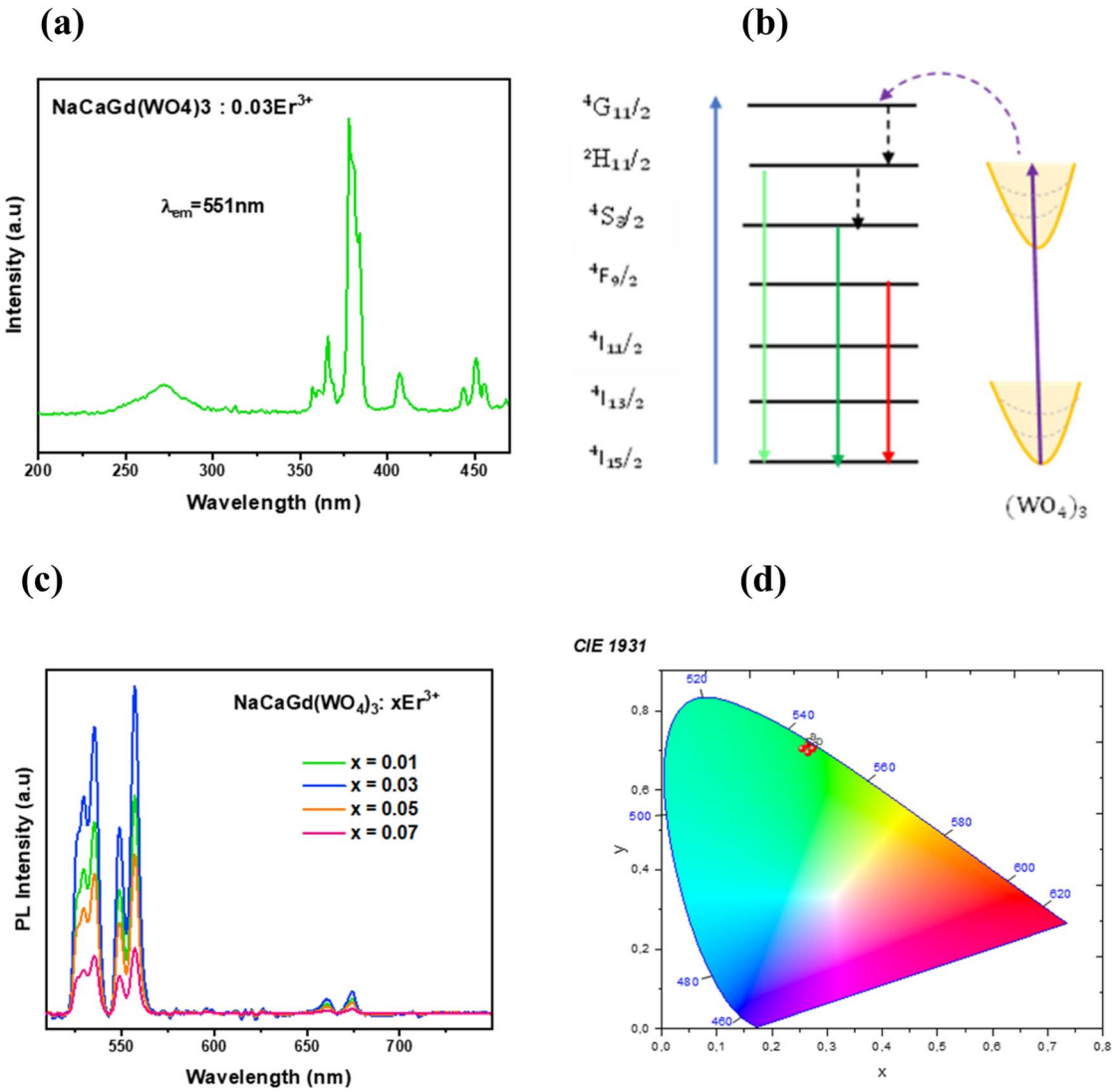

Fig. 6 (a) Photoluminescence excitation (PLE) spectrum of $NaCaGd(WO_4)_3$:3% Er^{3+} phosphor recorded at room temperature by monitoring the green emission at $\lambda_{em} = 551$ nm ($^4S_{3/2} \rightarrow {}^4I_{15/2}$ transition). The dominant excitation band at ~325 nm is assigned to the WO_4^{2-} charge-transfer transition, evidencing efficient host sensitization of Er^{3+} ions. (b) Schematic energy-level diagram illustrating the proposed host-to-Er^{3+} energy transfer mechanism under 325 nm excitation, followed by non-radiative relaxation and green emission from the thermally coupled $^2H_{11/2}$ and $^4S_{3/2}$ levels (down-conversion process). (c) Photoluminescence emission spectra of $NaCaGd(WO_4)_3$:xEr^{3+} ($x = 0.01$, 0.03, 0.05, and 0.07) under 325 nm excitation, showing concentration-dependent emission intensity and optimal luminescence at 3 mol% Er^{3+}. (d) Corresponding CIE 1931 chromaticity diagram derived from the emission spectra under 325 nm excitation, indicating saturated green emission and slight coordinate variations with increasing Er^{3+} concentration.

absolute sensitivity peaks at 1.8×10^{-2} K^{-1} at 500 K. As show in Fig. 7c. Beyond sensitivity, temperature resolution (δT) defined as the minimum detectable temperature change is a critical figure of merit for practical thermometry applications. It is inversely proportional to the relative sensitivity and the measurement uncertainty of the LIR:

$$\delta T = \frac{1}{S_r} \times \frac{\delta \mathrm{LIR}}{\mathrm{LIR}} \quad (5)$$

where δ(LIR)/LIR represents the relative uncertainty in the intensity ratio measurement. To determine the practical detection limit, the temperature resolution (δT) was estimated using eqn (5).

The relative uncertainty in the luminescence intensity ratio (δ(LIR)/LIR) was conservatively assessed at 5%, based on the signal-to-noise ratio and reproducibility of repeated PL measurements under identical conditions.[31,32,49,50] This level of uncertainty is consistent with typical ratiometric luminescence thermometry protocols. The calibration curve obtained from the LIR approach in $NaCaGd(WO_4)_3$:Er^{3+} is highly precise and reliable, with a minimum δT of 0.14 K at 300 K, which increases to 0.7 K at 573 K due to a decline in relative sensitivity (S_r) at higher temperatures. Additionally, the method is inherently self-referencing, as it relies on the ratio of two emission bands from the same Er^{3+} ion.

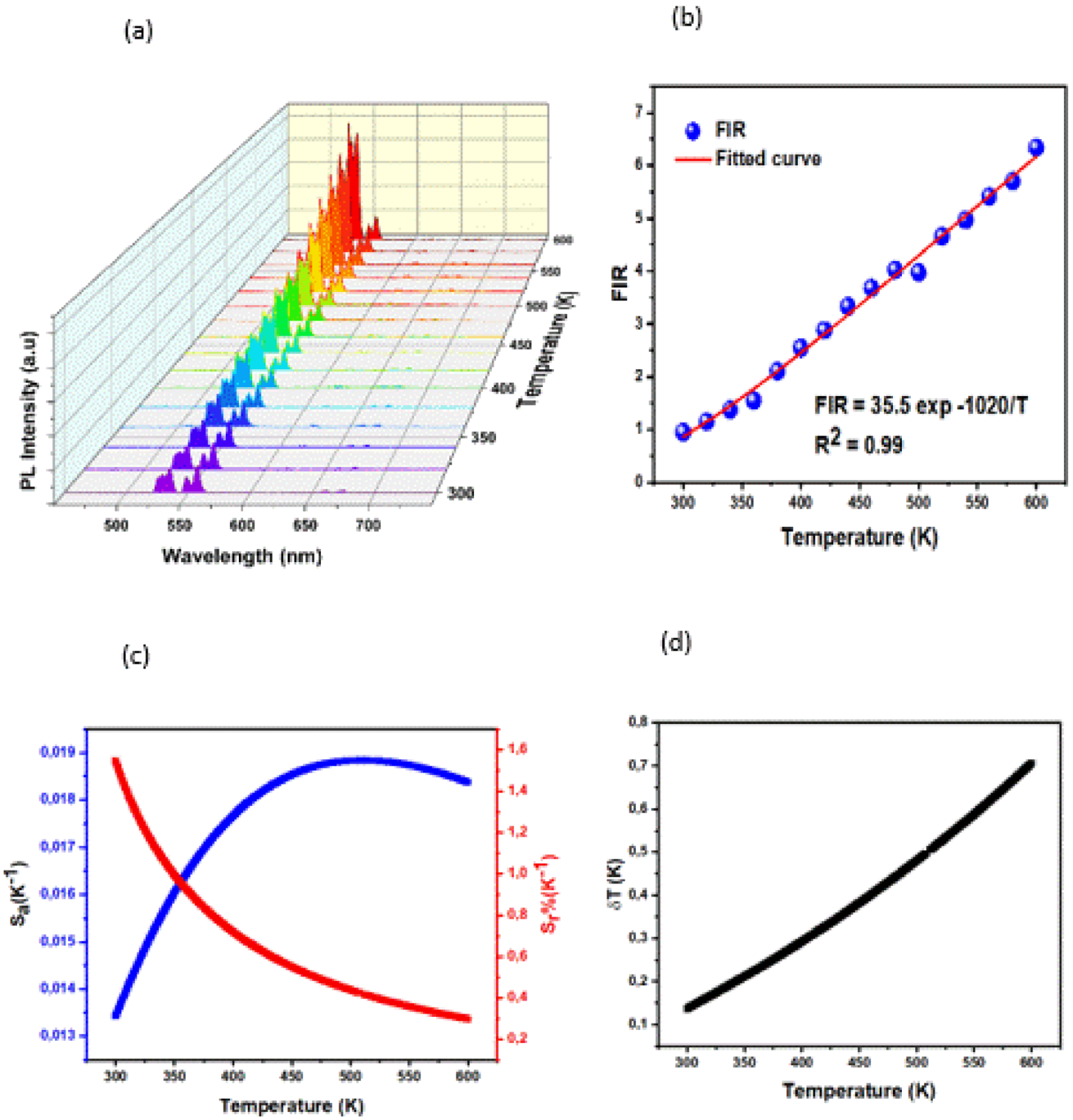

Fig. 7 Temperature-dependent optical thermometric behavior of $NaCaGd(WO_4)_3$:3% Er^{3+} phosphor in the 298–573 K range. (a) Down-conversion photoluminescence emission spectra recorded under 325 nm excitation at different temperatures, showing the thermally induced redistribution of populations between the $^2H_{11/2}$ and $^4S_{3/2}$ levels of Er^{3+}. (b) Fluorescence intensity ratio (FIR) plotted as a function of temperature, together with the Boltzmann fitting curve confirming thermally coupled levels behavior. (c) Temperature dependence of the calculated absolute sensitivity (S_a) and relative sensitivity (S_r), highlighting maximum sensitivity near room temperature. (d) Corresponding temperature resolution (δT) derived from FIR analysis, demonstrating high measurement precision over the investigated temperature range.

The thermometric performance of the synthesized $NaCaGd(WO_4)_3$:Er^{3+} phosphor was systematically compared with representative Er^{3+}-doped and Er^{3+}/Yb^{3+} co-doped optical thermometers from the recent literature. The comparison, summarized in Table 1, focuses on the most relevant figures of merit for optical temperature sensing, namely the operating temperature range (ΔT), the maximum absolute sensitivity (S_a), and the maximum relative sensitivity (S_r). This benchmarking

Table 1 Comparative thermometric performance of Er^{3+}-based optical thermometers reported in various host lattices

Host matrix	Dopants	Excitation (λ_{ex})	Temperature range (K)	S_{aMax} (K^{-1})	S_{rMax} (% K^{-1})	Ref.
$NaCaGd(WO_4)_3$	Er^{3+}	325 nm	298–573	1.8×10^{-2}	1.55	This work
$NaSrGd(MoO_4)_3$	Er^{3+}	375 nm	298–488	3.6×10^{-3}	0.87	40
$NaGd(WO_4)_2$	Er^{3+}/Yb^{3+}	980 nm	300–550	6.3×10^{-3}	1.15	17
$CaWO_4$	Er^{3+}/Yb^{3+}	980 nm	294–923	9.2×10^{-3}	1.12	13
β-$NaYF_4$	Er^{3+}/Yb^{3+}	980 nm	303–483	3.5×10^{-3}	1.14	51
Y_2O_3	Er^{3+}/Yb^{3+}	980 nm	298–573	4.8×10^{-3}	1.02	52
$NaGd(MoO_4)_2$	Er^{3+}/Yb^{3+}	980 nm	298–500	1.2×10^{-2}	1.25	53
Gd_2O_3	Er^{3+}/Yb^{3+}	980 nm	300–900	4.5×10^{-3}	1.10	54
$BaMoO_4$	Er^{3+}/Yb^{3+}	980 nm	300–530	7.8×10^{-3}	1.19	55
$CaLaAlO_4$	Er^{3+}/Yb^{3+}	980 nm	313–573	3.4×10^{-3}	1.28	56

contextualizes the performance of the present material within the broader landscape of rare-earth-based luminescent thermometers employing different host matrices and excitation schemes.

The comparative analysis presented in Table 1 situates the thermometric performance of Er^{3+}:$NaCaGd(WO_4)_3$ within the current state of the art and reveals several key advantages. Most notably, the material exhibits a high maximum relative sensitivity of 1.55% K^{-1} near room temperature, which clearly surpasses the values reported for widely used benchmark systems such as β-$NaYF_4$:Er^{3+}/Yb^{3+} (1.14% K^{-1}) and Y_2O_3:Er^{3+}/Yb^{3+} (1.02% K^{-1}), as well as chemically related tungstate hosts including $NaGd(WO_4)_2$:Er^{3+}/Yb^{3+} (1.15% K^{-1}). This enhanced sensitivity in the 298–310 K range is particularly advantageous for applications requiring the detection of subtle temperature variations at high resolution. In addition, unlike most high-performance optical thermometers that rely on Yb^{3+} sensitization and near-infrared excitation, the present system achieves competitive thermometric figures of merit using Er^{3+} as the sole optically active ion, thereby simplifying material design, reducing compositional complexity, and mitigating energy back-transfer or cross-relaxation effects commonly observed in Er^{3+}/Yb^{3+} co-doped systems. The ability to efficiently excite Er^{3+}:$NaCaGd(WO_4)_3$ at 325 nm further enhances its technological relevance, as near-UV LEDs are compact, energy-efficient, and readily available, facilitating integration into portable and low-cost sensing platforms without the need for specialized infrared laser sources. Moreover, the broad operating temperature range of 298–573 K effectively bridges both biological and industrial sensing regimes, while the intrinsic thermal robustness of the tungstate host ensures stable and reliable performance under elevated-temperature or otherwise demanding operating conditions.

5 Conclusion

This study establishes Er^{3+}-doped $NaCaGd(WO_4)_3$ as a robust multifunctional phosphor combining structural integrity, efficient green emission, and reliable optical thermometry performance. Rietveld-refined X-ray diffraction, complemented by SEM analysis, confirms the successful incorporation of Er^{3+} ions into the tetragonal scheelite lattice without detectable secondary phases, accompanied by a slight and systematic lattice contraction.

Under 325 nm excitation corresponding to the WO_4^{2-} charge-transfer band, the phosphor exhibits intense green photoluminescence, with optimal emission achieved at an Er^{3+} concentration of 3 mol%, dominated by the characteristic $^2H_{11/2} \rightarrow {}^4I_{15/2}$ and $^4S_{3/2} \rightarrow {}^4I_{15/2}$ transitions centered at 528 and 551 nm. The strong excitation efficiency under host-band pumping, together with the absence of residual host emission, indicates effective host-sensitized excitation of Er^{3+} ions. The resulting CIE chromaticity coordinates (0.337, 0.587) lie in the saturated green region, underscoring the suitability of this material for solid-state lighting driven by near-UV LED sources.

Furthermore, the thermally coupled $^2H_{11/2}$ and $^4S_{3/2}$ excited states enable accurate fluorescence intensity ratio (FIR)-based thermometry over a broad temperature range (298–573 K), delivering a maximum relative sensitivity of 1.55% K^{-1} and an absolute sensitivity of 1.8×10^{-2} K^{-1} near 298 K, together with a temperature resolution of 0.15 K at room temperature. The ratiometric detection scheme ensures intrinsic resistance to excitation power fluctuations and optical losses, thereby enhancing measurement reliability.

Overall, the demonstrated phase purity, strong green emission, and competitive thermometric figures of merit position Er^{3+}:$NaCaGd(WO_4)_3$ as a promising candidate for phosphor-converted LEDs and non-contact optical temperature sensing in technologically relevant environments. Future time-resolved investigations may provide deeper insight into the dynamics of host-to-dopant energy transfer.

Conflicts of interest

There are no conflicts to declare.

Data availability

All data underlying the results are available as part of the article and no additional source data are required.

References

1 M. Bettinelli, L. Carlos and X. Liu, Lanthanide-doped upconversion nanoparticles, *Phys. Today*, 2015, **68**, 38–44, DOI: 10.1063/PT.3.2913.

2 J.-C. G. Bünzli, Lanthanide Photonics: Shaping the Nanoworld, *Trends Chem.*, 2019, **1**, 751–762, DOI: 10.1016/j.trechm.2019.05.012.

3 E. Vorathin, Z. M. Hafizi, N. Ismail and M. Loman, Review of high sensitivity fibre-optic pressure sensors for low pressure sensing, *Opt. Laser Technol.*, 2020, **121**, 105841, DOI: 10.1016/j.optlastec.2019.105841.

4 P. Du, L. Luo, H.-K. Park and J. S. Yu, Citric-assisted sol-gel based Er3+/Yb3+-codoped Na0.5Gd0.5MoO4: A novel highly-efficient infrared-to-visible upconversion material for optical temperature sensors and optical heaters, *Chem. Eng. J.*, 2016, **306**, 840–848, DOI: 10.1016/j.cej.2016.08.007.

5 P. Du and J. S. Yu, NUV light-induced-visible emissions and dopant concentration-dependent optical thermometric behaviors in Y2Mo4O15:2xEr3+ phosphors, *J. Alloys Compd.*, 2018, **767**, 724–732, DOI: 10.1016/j.jallcom.2018.07.143.

6 P. Du, L. Luo and J. S. Yu, Energy Back Transfer Induced Color Controllable Upconversion Emissions in La2MoO6:Er3+/Yb3+ Nanocrystals for Versatile Applications, *Part. Part. Syst. Charact.*, 2018, **35**, 1700416, DOI: 10.1002/ppsc.201700416.

7 K. Saidi, C. Hernández-Álvarez, M. Runowski, M. Dammak and I. R. Martín, Ultralow pressure sensing and luminescence thermometry based on the emissions of Er3+/Yb3+ codoped Y2Mo4O15 phosphors, *Dalton Trans.*, 2023, **52**, 14904–14916, DOI: 10.1039/D3DT02613B.

8 T. Zheng, M. Runowski, N. Stopikowska, M. Skwierczyńska, S. Lis, P. Du and L. Luo, Dual-center thermochromic Bi2MoO6:Yb3+, Er3+, Tm3+ phosphors for ultrasensitive luminescence thermometry, *J. Alloys Compd.*, 2022, **890**, 161830, DOI: 10.1016/j.jallcom.2021.161830.

9 M. Runowski, A. Shyichuk, A. Tymiński, T. Grzyb, V. Lavín and S. Lis, Multifunctional Optical Sensors for Nanomanometry and Nanothermometry: High-Pressure and High-Temperature Upconversion Luminescence of Lanthanide-Doped Phosphates—LaPO $_4$/YPO $_4$:Yb $^{3+}$ –Tm $^{3+}$, *ACS Appl. Mater. Interfaces*, 2018, **10**, 17269–17279, DOI: 10.1021/acsami.8b02853.

10 M. Runowski, P. Woźny and I. R. Martín, Optical pressure sensing in vacuum and high-pressure ranges using lanthanide-based luminescent thermometer–manometer, *J. Mater. Chem. C*, 2021, **9**, 4643–4651, DOI: 10.1039/D1TC00709B.

11 Y. Ding, B. So, J. Cao, F. Langenhorst and L. Wondraczek, Light Delivery, Acoustic Read-Out, and Optical Thermometry Using Ultrasound-Induced Mechanoluminescence and the Near-Infrared Persistent Luminescence of CaZnOS:Nd3+, *Adv. Opt. Mater.*, 2023, **11**(17), 2300331, DOI: 10.1002/adom.202300331.

12 R. G. Geitenbeek, B. B. V. Salzmann, A.-E. Nieuwelink, A. Meijerink and B. M. Weckhuysen, Chemically and thermally stable lanthanide-doped Y2O3 nanoparticles for remote temperature sensing in catalytic environments, *Chem. Eng. Sci.*, 2019, **198**, 235–240, DOI: 10.1016/j.ces.2018.10.004.

13 X. Bai, Y. Cun, Z. Xu, Y. Zi, A. A. Haider, A. Ullah, I. Khan, J. Qiu, Z. Song and Z. Yang, Multiple Anti-Counterfeiting and optical storage of reversible dual-mode luminescence modification in photochromic CaWO4: Yb3+, Er3+, Bi3+ phosphor, *Chem. Eng. J.*, 2022, **429**, 132333, DOI: 10.1016/j.cej.2021.132333.

14 K. Saidi, M. Yangui, C. Hernández-Álvarez, M. Dammak, I. Rafael Martín Benenzuela and M. Runowski, Multifunctional Optical Sensing with Lanthanide-Doped Upconverting Nanomaterials: Improving Detection Performance of Temperature and Pressure in the Visible and NIR Ranges, *ACS Appl. Mater. Interfaces*, 2024, **16**, 19137–19149, DOI: 10.1021/acsami.4c00313.

15 X. Chai, J. Li, Y. Zhang, X. Wang, Y. Li and X. Yao, Bright dual-mode green emission and temperature sensing properties in Er $^{3+}$/Yb $^{3+}$ co-doped MgWO $_4$ phosphor, *RSC Adv.*, 2016, **6**, 64072–64078, DOI: 10.1039/C6RA09656E.

16 Y. Liu, Y. Liu, G. Liu, X. Dong and J. Wang, Up/down conversion, tunable photoluminescence and energy transfer properties of NaLa(WO 4) 2 :Er 3+ ,Eu 3+ phosphors, *RSC Adv.*, 2015, **5**, 97995–98003, DOI: 10.1039/C5RA17370A.

17 J. Liao, L. Nie, Q. Wang, S. Liu, H.-R. Wen and J. Wu, NaGd(WO4)2:Yb3+/Er3+ phosphors: hydrothermal synthesis, optical spectroscopy and green upconverted temperature sensing behavior, *RSC Adv.*, 2016, **6**, 35152–35159, DOI: 10.1039/C6RA01283C.

18 K. Saidi, I. Kachou, K. Soler-Carracedo, M. Dammak and I. R. Martín, Ba2YV3O11 Er3+/Yb3+ Nanostructures for Temperature Sensing in the Presence of Bismuth Ions, *ACS Appl. Nano Mater.*, 2023, **6**(19), 17681–17690, DOI: 10.1021/acsanm.3c02911.

19 I. Kachou, Y. Bahrouni, K. Saidi, M. Dammak, I. Mediavilla and J. Jiménez, Dual-mode optical thermometry based on up- and down-conversion photoluminescence in LiCaLa(MoO 4) 3 :Er 3+/Yb 3+ phosphors with high sensitivity, *RSC Adv.*, 2025, **15**, 28428–28438, DOI: 10.1039/D5RA05181A.

20 W. Wu, Y. Xu, X. Lin, F. Huang, Y.-N. Feng, L. Zhang, Y. Yu and L. Li, Ultra-Stable Er^{3+}/Yb^{3+} Co-Doped Scheelite Single Crystals for Wide-Range Fiber-Free Optical Thermometry, *J. Lumin.*, 2025, **283**, 121251, DOI: 10.1016/j.jlumin.2025.121251.

21 L. Zheng, *et al.*, Upconversion luminescence and temperature sensing properties of $NaGd(WO_4)_2$:Yb^{3+}/Er^{3+}@SiO_2 core–shell nanoparticles, *RSC Adv.*, 2021, **11**, 3981–3989, DOI: 10.1039/D0RA10039K.

22 N. Jurga, M. Runowski and T. Grzyb, Excitation and temperature sensing in optical transparency windows, *J. Mater. Chem. C*, 2024, **12**, 12218–12248, DOI: 10.1039/D3TC04716D.

23 F. Jahanbazia and Y. Mao, Recent advances on metal oxide-based luminescence thermometry, *J. Mater. Chem. C*, 2021, **9**, 16410–16439, DOI: 10.1039/D1TC03455C.

24 H. Yan, R. Li, L. Feng, Y. Yu, G. Gong, H. Huang, H.-R. Wen and J. Liao, Simultaneous negative thermal quenching luminescence of upconversion and downshifting processes in Al2(WO4)3:Yb/Er phosphors with low thermal expansion, *J. Mater. Chem. C*, 2024, **12**, 12353–12362, DOI: 10.1039/D4TC02102A.

25 J. N. Mohshin, S. M. T. Ahmed, A. R. Aidid, N. R. Sayeem, H. Yasmin, Md. A. Alam, J. Khanam, S. Ganguli and A. K. Chakraborty, Powder X-ray peak diffraction pattern of iron (II) tungstate (FeWO4): Crystallite size and strain analysis, and adsorption of methylene blue, *Nano-Struct. Nano-Objects*, 2025, **44**, 101574, DOI: 10.1016/j.nanoso.2025.101574.

26 N. Görener Erdem, Ö. Tuna, İ. F. Ertis and E. B. Simsek, Design of novel Z-scheme Ce2(WO4)3 heterostructure using tubular g-C3N4 for boosted photocatalytic performance via effective electron transfer pathway, *J. Mol. Struct.*, 2025, **1323**, 140736, DOI: 10.1016/j.molstruc.2024.140736.

27 P. V. Klevtsov and R. F. Klevtsova, Single-crystal synthesis and investigation of the double tungstates NaR3+(WO4)2, where R3+ = Fe, Sc, Ga, and In, *J. Solid State Chem.*, 1970, **2**, 278–282, DOI: 10.1016/0022-4596(70)90080-0.

28 B. Baby, A. V. Lizbathu, S. P. Nair, N. D. Abraham, V. Sudarsan, A. Gopinath, P. R. Biju and C. Joseph, Photoluminescence characteristics of microwave synthesized La2(WO4)3:Eu3+ phosphor and evaluation of its radiative parameters, *Ceram. Int.*, 2024, **50**, 11500–11509, DOI: 10.1016/j.ceramint.2024.01.050.

29 I. Trabelsi, M. Dammak, R. Maâlej and M. Kamoun, A general trend of rare earth ions in the KRE(WO4)2 double tungstates (RE=Y, Yb, Gd, Lu), *Mater. Sci. Eng., B*, 2010, **172**, 89–95, DOI: 10.1016/j.mseb.2010.04.023.

30 I. Kachou, K. Saidi, U. Ekim, M. Dammak, M. Ç. Ersundu and A. E. Ersundu, Advanced temperature sensing with Er3+/Yb3+ co-doped Ba2GdV3O11 phosphors through upconversion luminescence, *Dalton Trans.*, 2024, **53**, 2357–2372, DOI: 10.1039/D3DT04015A.

31 K. Saidi and M. Dammak, Upconversion luminescence and optical temperature sensing characteristics of Er3+/Yb3+ codoped Na3Gd(PO4)2 phosphors, *J. Solid State Chem.*, 2021, **300**, 122214, DOI: 10.1016/j.jssc.2021.122214.

32 K. Saidi, W. Chaabani and M. Dammak, Highly sensitive optical temperature sensing based on pump-power-dependent upconversion luminescence in LiZnPO 4 :Yb 3+ –Er 3+/Ho 3+ phosphors, *RSC Adv.*, 2021, **11**, 30926–30936, DOI: 10.1039/D1RA06049J.

33 H. X. Jiang and S. C. Lü, Intense red emission and two-way energy transfer in Sm3+, Eu3+ co-doped NaLa(WO4)2 phosphors, *Mater. Res. Bull.*, 2019, **111**, 140–145, DOI: 10.1016/j.materresbull.2018.11.004.

34 D. L. Shruthi, G. N. Anil Kumar and A. Jagannatha Reddy, Solid solution of novel LixByGdEu (WO4)2 (B=Na, K) red phosphors: Influence of Na/K substitution on microstructures, Judd-Ofelt and luminescence properties for WLED applications, *Ceram. Int.*, 2021, **47**, 16342–16357, DOI: 10.1016/j.ceramint.2021.02.214.

35 D. Manzani, J. F. da S. Petruci, K. Nigoghossian, A. A. Cardoso and S. J. L. Ribeiro, A portable luminescent thermometer based on green up-conversion emission of Er3+/Yb3+ co-doped tellurite glass, *Sci. Rep.*, 2017, **7**, 41596, DOI: 10.1038/srep41596.

36 C. Wang, P. Du, L. Luo and W. Li, Photocatalytic, thermometric and internal heating multifunctional properties of Er3+/Yb3+-codoped MoO3 upconverting microparticles, *J. Lumin.*, 2021, **233**, 117896, DOI: 10.1016/j.jlumin.2021.117896.

37 K. N. Kumar, G. Kang, J. Lim and J. Choi, Biocompatible Yb3+/Er3+ Co-activated La2(WO4)3 Upconversion Nanophosphors for Optical Thermometry, Biofluorescent, and Anticancer Agents, *Inorg. Chem.*, 2022, **61**, 3851–3865, DOI: 10.1021/acs.inorgchem.1c03296.

38 C. S. Lim, A. Aleksandrovsky, M. Molokeev, A. Oreshonkov and V. Atuchin, Microwave sol–gel synthesis and upconversion photoluminescence properties of CaGd2(WO4)4:Er3+/Yb3+ phosphors with incommensurately modulated structure, *J. Solid State Chem.*, 2015, **228**, 160–166, DOI: 10.1016/j.jssc.2015.04.032.

39 F. Ayachi, K. Saidi, W. Chaabani and M. Dammak, Synthesis and luminescence properties of Er3+ doped and Er3+–Yb3+ codoped phosphovanadate YP0.5V0.5O4 phosphors, *J. Lumin.*, 2021, **240**, 118451, DOI: 10.1016/j.jlumin.2021.118451.

40 Z. E. A. A. Taleb, K. Saidi and M. Dammak, The dual-model up/down-conversion green luminescence of NaSrGd(MoO 4) 3 : Er 3+ and its application for temperature sensing, *RSC Adv.*, 2024, **14**, 8366–8377, DOI: 10.1039/D4RA00934G.

41 O. Shchekin and M. G. Craford, History of Solid-State Light Sources, in *Handbook of Advanced Lighting Technology*, ed. R. Karlicek, C.-C. Sun, G. Zissis and R. Ma, Springer International Publishing, Cham, 2017, pp. 1–30, DOI: 10.1007/978-3-319-00295-8_63-2.

42 J. Xue, M. Song, H. M. Noh, S. H. Park, B. R. Lee, J. H. Kim and J. H. Jeong, Near-ultraviolet light induced red emission in Sm3+-activated NaSrLa(MoO4)O3 phosphors for solid-state illumination, *J. Alloys Compd.*, 2020, **817**, 152705, DOI: 10.1016/j.jallcom.2019.152705.

43 W. Ran, H. M. Noh, S. H. Park, B. R. Lee, J. H. Kim, J. H. Jeong, J. Shi and G. Liu, Simultaneous bifunctional application of solid-state lighting and ratiometric optical thermometer based on double perovskite LiLaMgWO $_6$:Er $^{3+}$ thermochromic phosphors, *RSC Adv.*, 2019, **9**, 7189–7195, DOI: 10.1039/C8RA10242B.

44 R. Galvão, L. F. dos Santos, K. de O. Lima, R. R. Gonçalves and L. de S. Menezes, Single Er3+/Yb3+-Codoped Yttria Nanocrystals for Temperature Sensing: Experimental Characterization and Theoretical Modeling, *J. Phys. Chem. C*, 2021, **125**, 14807–14817, DOI: 10.1021/acs.jpcc.1c03058.

45 P. Du, L. Luo, X. Huang and J. S. Yu, Ultrafast synthesis of bifunctional Er3+/Yb3+-codoped NaBiF4 upconverting nanoparticles for nanothermometer and optical heater, *J.*

Colloid Interface Sci., 2018, **514**, 172–181, DOI: 10.1016/j.jcis.2017.12.027.

46 Y. Chen, J. He, X. Zhang, M. Rong, Z. Xia, J. Wang and Z.-Q. Liu, Dual-Mode Optical Thermometry Design in $Lu_3Al_5O_{12}:Ce^{3+}/Mn^{4+}$ Phosphor, *Inorg. Chem.*, 2020, **59**, 1383–1392, DOI: 10.1021/acs.inorgchem.9b03107.

47 D. K. Amarasinghe and F. A. Rabuffetti, Ratiometric Thermometry Using Thermochromic $Tb^{3+}:Mn^{4+}:Na_4Mg(WO_4)_3$ Phosphors, *Inorg. Chem.*, 2021, **60**, 3165–3171, DOI: 10.1021/acs.inorgchem.0c03513.

48 A. F. Pereira, K. U. Kumar, W. F. Silva, W. Q. Santos, D. Jaque and C. Jacinto, Yb3+/Tm3+ co-doped NaNbO3 nanocrystals as three-photon-excited luminescent nanothermometers, *Sens. Actuators, B*, 2015, **213**, 65–71, DOI: 10.1016/j.snb.2015.01.136.

49 A. A. Ansari, A. K. Parchur, M. K. Nazeeruddin and M. M. Tavakoli, Luminescent lanthanide nanocomposites in thermometry: Chemistry of dopant ions and host matrices, *Coord. Chem. Rev.*, 2021, **444**, 214040, DOI: 10.1016/j.ccr.2021.214040.

50 C. D. S. Brites, A. Millán and L. D. Carlos, Lanthanides in Luminescent Thermometry, in *Handbook on the Physics and Chemistry of Rare Earths*, Elsevier, 2016, pp. 339–427, DOI: 10.1016/bs.hpcre.2016.03.005.

51 L. Tong, X. Li, J. Zhang, S. Xu, J. Sun, L. Cheng, H. Zheng, Y. Zhang, X. Zhang, R. Hua, H. Xia and B. Chen, Microwave-assisted hydrothermal synthesis, temperature quenching and laser-induced heating effect of hexagonal microplate β-NaYF4: Er3+/Yb3+ microcrystals under 1550 nm laser irradiation, *Sens. Actuators, B*, 2017, **246**, 175–180, DOI: 10.1016/j.snb.2017.02.030.

52 G. Chen, H. Liu, H. Liang, G. Somesfalean and Z. Zhang, Upconversion Emission Enhancement in Yb3+/Er3+-Codoped Y2O3 Nanocrystals by Tridoping with Li+ Ions, *J. Phys. Chem. C*, 2008, **112**, 12030–12036, DOI: 10.1021/jp804064g.

53 A. Li, D. Xu, H. Lin, L. Yao, S. Yang, Y. Shao, Y. Zhang and Z. Chen, A novel anion doping strategy to enhance upconversion luminescence in $NaGd(MoO_4)_2:Yb^{3+}/Er^{3+}$ nanophosphors, *Phys. Chem. Chem. Phys.*, 2017, **19**, 15693–15700, DOI: 10.1039/C7CP00855D.

54 S. K. Ranjan, M. Mondal and V. K. Rai, Er3+-Yb3+/Er3+-Yb3+-Li+/Er3+-Yb3+-Zn2+:Gd2O3 nanophosphors for efficient frequency upconverter and temperature sensing applications, *Mater. Res. Bull.*, 2018, **106**, 66–73, DOI: 10.1016/j.materresbull.2018.05.023.

55 A. K. Soni and V. K. Rai, Promising light converting BaMoO4:Er3+-Tm3+-Yb3+ phosphors for display and optical temperature sensing, *J. Rare Earths*, 2018, **36**, 1256–1263, DOI: 10.1016/j.jre.2018.03.034.

56 P. Gao, X. Li, Y. Gong, G. Shen, S. Zhang and L. Guan, Highly sensitive up-conversion phosphor for optical thermometry: CaLaAl3O7:Er3+/Yb3+, *J. Rare Earths*, 2019, **37**, 937–942, DOI: 10.1016/j.jre.2018.12.005.